Anomalous double-stripe charge ordering in β-$NaFe_2O_3$ with double triangular layers consisting of almost perfect regular Fe_4 tetrahedra

Shintaro Kobayashi,[1,*] Hiroaki Ueda,[2] Chishiro Michioka,[2] Kazuyoshi Yoshimura,[2,3] Shin Nakamura,[4,5] Takuro Katsufuji,[6] and Hiroshi Sawa[1]

[1]*Department of Applied Physics, Graduate School of Engineering, Nagoya University, Nagoya 464-8603, Japan*
[2]*Department of Chemistry, Graduate School of Science, Kyoto University, Kyoto 606-8502, Japan*
[3]*Research Center for Low Temperature and Material Sciences, Kyoto University, Kyoto 606-8501, Japan*
[4]*Department of Science and Engineering, Teikyo University, Utsunomiya 320-8551, Japan*
[5]*Advanced Research Institute of Science and Engineering, Waseda University, Shinjuku, Tokyo 169-8555, Japan*
[6]*Faculty of Science and Engineering, Waseda University, Shinjuku, Tokyo 169-8555, Japan*

(Received 28 February 2018; published 7 May 2018)

The physical properties of the mixed-valent iron oxide β-$NaFe_2O_3$ were investigated by means of synchrotron radiation x-ray diffraction, magnetization, electrical resistivity, differential scanning calorimetry, ^{23}Na NMR, and ^{57}Fe Mössbauer measurements. This compound has double triangular layers consisting of almost perfect regular Fe_4 tetrahedra, which suggests geometrical frustration. We found that this compound exhibits an electrostatically unstable double-stripe-type charge ordering, which is stabilized by the cooperative compression of $Fe^{3+}O_6$ octahedra, owing to a valence change and $Fe^{2+}O_6$ octahedra due to Jahn-Teller distortion. Our results indicate the importance of electron-phonon coupling for charge ordering in the region of strong charge frustration.

DOI: 10.1103/PhysRevMaterials.2.054402

I. INTRODUCTION

Antiferromagnets with triangular and pyrochlore lattices have been intensively studied because they have the potential to exhibit exotic ground states realized by the influence of spin frustration [1–4]. Mixed-valent oxides are expected to exhibit electrostatically stable charge ordering (Wigner crystallization) mediated by long-range Coulomb repulsions. However, in the case of geometrically frustrated systems, exotic electronic states, such as exotic charge ordering (CO), charge glasses, and charge liquids, are expected to originate from "charge frustration" [5–9]. Specifically, mixed-valent pyrochlore oxides often show electrostatically unstable CO patterns [10–13]. One well-known example is magnetite Fe_3O_4, where parts of the Fe_4 tetrahedra in its CO pattern do not satisfy the local charge neutrality condition (Anderson's condition) that a Fe_4 tetrahedron should contain two Fe^{2+} and two Fe^{3+} ions [14–20]. If the tetrahedral topology consisting of mixed-valent ions plays an important role in unusual CO phenomena, exotic CO states are also expected in other geometrically frustrated systems with tetrahedral frameworks.

Mixed-valent oxides with double triangular layers (W layers) have characteristic tetrahedral frameworks and are one of the ideal candidates to study the effects of charge frustration on tetrahedra. A W layer consists of a set of two regular triangular sheets as shown in Fig. 1(b). The geometric relationship of interactions among metal ions within a W layer is classified by the local symmetry. Figure 1(a) exhibits the definition of the interlayer distance h within a W layer and the side length l_1 of regular triangles. In the condition $h/l_1 = \sqrt{2/3}$, l_1 is equal to the interplane nearest-neighbor metal-metal distance l_2 within a W layer, and thus, the W layer consists of regular tetrahedra. For $h/l_1 \ll \sqrt{2/3}$, l_2 is shorter than l_1, and the geometric relation of the W layer gets closer to that of a honeycomb lattice, in which geometrical frustration is eliminated. For $h/l_1 \gg \sqrt{2/3}$, interplane interactions between triangular sheets become weak, and the geometrical configuration gets closer to a triangular lattice. Thus, the system is suitable to systematically study the effects of charge frustration by controlling the distortion of tetrahedra. One famous example is $LuFe_2O_4$ [21–30] with $l_2/l_1 \sim 0.9$, which exhibits large dielectric constants arising from polar CO.

The mixed-valent oxide β-$NaFe_2O_3$ is one of the candidates having W layers consisting of almost perfect regular Fe_4 tetrahedra. Figure 1(c) shows a crystal structure of β-$NaFe_2O_3$. There is one crystallographic Fe site with mixed valence of +2.5, and l_2/l_1 is very close to 1 [31–33], which suggests charge frustration. The arrangement of Fe ions in β-$NaFe_2O_3$ is similar to that in $LuFe_2O_4$, whose unusual valence ordering with ferroelectricity is still controversial [21–30]. In contrast, the coordination environment of Fe ions is different, forming FeO_6 octahedra for β-$NaFe_2O_3$ and FeO_5 bipyramids for $LuFe_2O_4$. Since it is easy to consider the effects of orbital degrees of freedom for simple FeO_6 octahedra, β-$NaFe_2O_3$ is suitable to investigate charge degrees of freedom on Fe_4 tetrahedra. However, there are no reports on its physical properties.

In this paper, we report on the physical properties and low-temperature structure of β-$NaFe_2O_3$. Charge ordering and magnetic ordering occur at 250 K and 230 K, respectively. The results of careful structural analysis show the formation of a local electrostatically unstable double-stripe CO pattern, and its origin is discussed.

*kobayashi.shintaro@b.mbox.nagoya-u.ac.jp

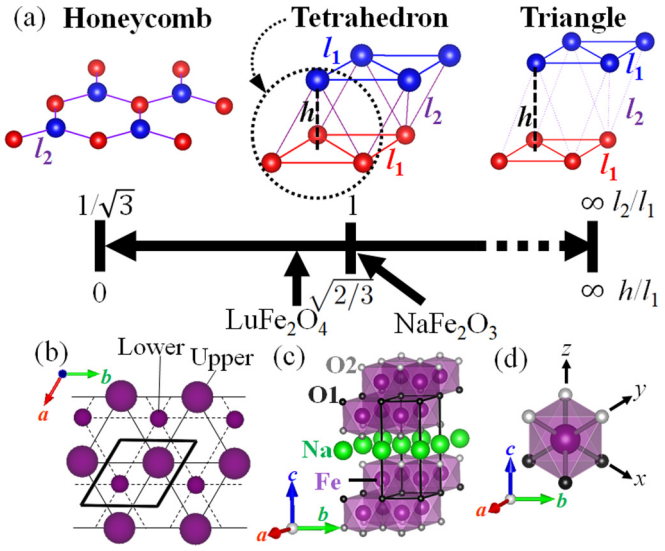

FIG. 1. (a) Geometric frameworks of a double triangular layer. (b) A double triangular layer. Large and small balls indicate atoms in upper and lower sheets, respectively. Bold solid lines indicate the unit cell. (c) Crystal structure of β-$NaFe_2O_3$. (d) FeO_6 octahedron. The quantization axis (z axis) is defined as the direction of a Fe-O bond.

II. EXPERIMENTAL METHODS

Polycrystalline samples of β-$NaFe_2O_3$ were prepared from high-purity β-$NaFeO_2$, α-Fe_2O_3, and Fe using a solid-state reaction similar to those of previous reports [31]. β-$NaFeO_2$ was synthesized by heating stoichiometric mixtures of $Na_2C_2O_4$ and α-Fe_2O_3 under an oxygen stream at 750°C. Fe powder was prepared by the reduction of α-Fe_2O_3 under a hydrogen stream at 500°C. High quality polycrystalline samples of β-$NaFe_2O_3$ were synthesized using a solid-state reaction. The mixture of stoichiometric amounts of β-$NaFeO_2$, α-Fe_2O_3, and Fe was pressed into a pellet, placed in an Au crucible, and sealed in a silica tube under a N_2 atmosphere. Next, they were heated at 700°C for 24 h, and then rapidly cooled in a water bath. The obtained samples were very sensitive to air, and thus, they were not exposed to air during the preparation or measurement.

Synchrotron radiation x-ray diffraction (SR-XRD) profiles of powder samples were collected using a high-resolution one-dimensional solid-state detector (MYTHEN) at the BL02B2 beamline of SPring-8 ($\lambda = 0.4964$ or 0.7981 Å) [34]. The samples were sealed in a glass capillary with a diameter of 0.2 mm in a N_2 atmosphere. DC magnetization was measured in a magnetic properties measurement system (Quantum Design MPMS-XL system). Electrical resistivity was measured using a conventional four-probe method. Differential scanning calorimetry (DSC) was performed (NETZSCH DSC 204F1 Phoenix). ^{23}Na (spin $I = 3/2$) nuclear magnetic resonance (NMR) spectra were collected at 6 T for sintered polycrystalline samples using a standard phase-coherent-type pulsed spectrometer. Frequency-swept NMR spectra were obtained by using a spin-echo method. ^{57}Fe Mössbauer spectra were measured in conventional transmission geometry using ^{57}Co-in-Rh (25 mCi) as the γ-ray source. A powder specimen, which was sealed in an acrylic cell, was used as an absorber. The Doppler velocity scale was calibrated with respect to Fe-metal foil. Lorentzian line shapes were assumed for the spectrum analysis. Parts of the analysis procedure for NMR and Mössbauer measurements are described in the Supplemental Material [35].

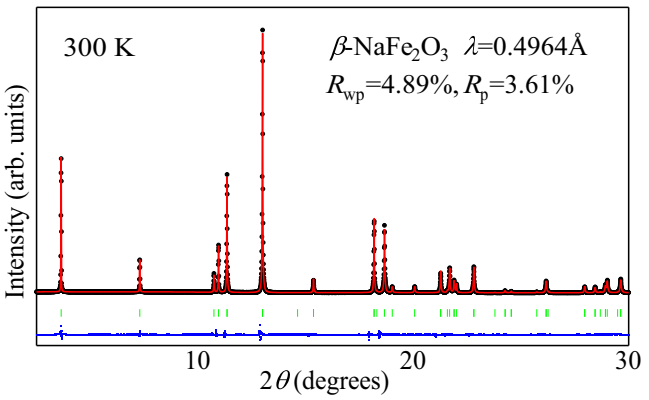

FIG. 2. The synchrotron x-ray diffraction pattern of polycrystalline samples of β-$NaFe_2O_3$ measured at 300 K and the Rietveld fit. Black dots: observed data. Red curve: calculated profile. Green tick marks: positions of reflections. Blue dots: differences.

III. RESULTS AND DISCUSSION

A. Physical properties

Although there are several reports on the difficulty of this synthesis [31–33], we successfully obtained high-quality black polycrystalline samples of β-$NaFe_2O_3$. As shown in Fig. 2, SR-XRD profiles obtained at 300 K were well reproduced using the previously reported structural model with the trigonal space group $P\bar{3}m1$ [31–33]. The lattice parameters at 300 K were $a = 3.061173(5)$ Å, and $c = 7.80045(2)$ Å. The result of refinements at 300 K is shown in Table I. The ratio l_2/l_1 was equal to 1.03, indicating the occurrence of strong frustration effects on Fe_4 tetrahedra.

Clear anomalies were observed at $T_{t1} = 250$ K in the temperature dependence of electrical resistivity ρ and DSC signals of β-$NaFe_2O_3$ as shown in Fig. 3(a). ρ increases with decreasing temperature T over the whole temperature range. At T_{t1}, ρ exhibits a clear jump with a thermal hysteresis, indicating a first-order transition. The activation energy increases slightly from 0.12 eV ($T > T_{t1}$) to 0.13 eV ($T < T_{t1}$). A large entropy change $\Delta S \simeq 2.8\,\mathrm{J/K \cdot molFe}$ was observed at T_{t1} in DSC signals. ^{57}Fe Mössbauer spectra also exhibit a drastic change

TABLE I. Refined structural parameters for β-$NaFe_2O_3$ at 300 K determined using synchrotron x-ray diffraction patterns. The space group is $P\bar{3}m1$, and the obtained lattice parameters are $a = 3.061173(5)$ Å, and $c = 7.80045(2)$ Å. The obtained R factors are $R_{wp} = 4.89\%$, $R_p = 3.61\%$.

Atom	Site	x	y	z	B (Å^2)
Na	1b	0	0	1/2	0.68(2)
Fe	2d	1/3	2/3	0.1672(1)	0.55(2)
O1	1a	0	0	0	1.36(4)
O2	2d	1/3	2/3	0.7056(2)	0.74(2)

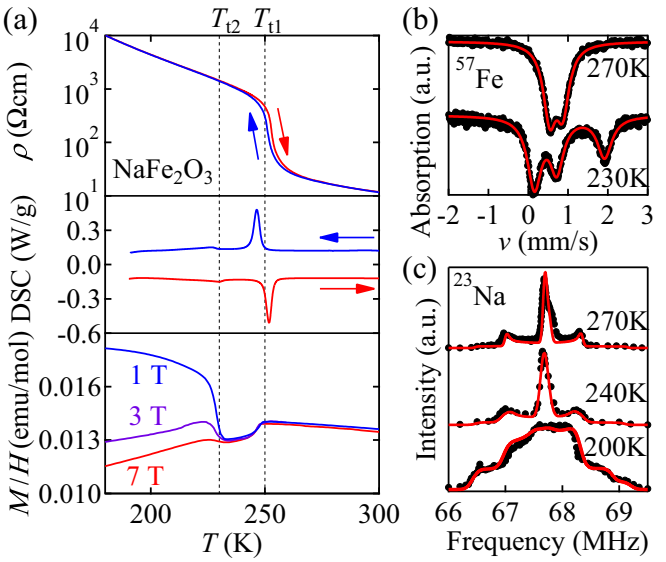

FIG. 3. (a) Temperature dependence of electrical resistivity (top panel), differential scanning calorimetry signals (middle panel), and magnetic susceptibility (bottom panel) of β-$NaFe_2O_3$. Arrows indicate heating and cooling directions. (b)^{57}Fe Mössbauer spectra of β-$NaFe_2O_3$. (c)^{23}Na NMR spectra of β-$NaFe_2O_3$. Black circles and red curves indicate results of experiments and simulations, respectively.

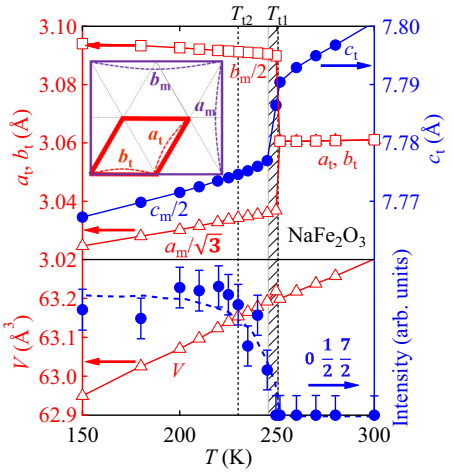

FIG. 4. Top panel: Temperature variation of lattice constants; inset shows the relation between the trigonal (red lines) and monoclinic (purple lines) unit cells. Between 245 K and 250 K, lattice parameters could not be determined correctly because of the coexistence of HT and IT phases. Bottom panel: Temperature dependence of the unit cell volume and the integrated intensity of superlattice reflection of 0 1/2 7/2 peak indexed with the trigonal cell. The error bars of the lattice constants and the unit cell volume are smaller than the corresponding symbols. The dotted lines are visual guides.

approximately at T_{t1}. Typical Mössbauer spectra are shown in Fig. 3(b). The Mössbauer spectra at 270 K and 230 K exhibit quadrupole splitting originating from the noncubic symmetry of Fe sites. The spectrum at 270 K consists of a paramagnetic quadrupole doublet with the isomer shift of 0.7 mm/s, which is a typical value for high-spin $Fe^{2.5+}$. The Mössbauer spectrum at 230 K was reproduced by two paramagnetic quadrupole doublets of almost equal intensity. Their isomer shifts are 0.4 and 1.0 mm/s, which are consistent with typical values of Fe^{3+} and Fe^{2+}, respectively. While the value of quadrupole splitting for $Fe^{2.5+}$ at 270 K is 0.3 mm/s, those for Fe^{3+} and Fe^{2+} at 230 K are 0.6 and 1.8 mm/s, respectively. The values for $Fe^{2.5+}$ and Fe^{3+} are reasonable for slightly distorted FeO_6 octahedra, and the large value for Fe^{2+} is due to the electric field gradient originating from the single extra electron outside the half-filled d shell. From the above results, we conclude that the transition at T_{t1} originates from CO.

Above T_{t1}, the ρ of β-$NaFe_2O_3$ is semiconducting rather than metallic in spite of the mixed-valent state. Although extrinsic effects such as grain boundary scattering in polycrystals often cause semiconductor-like temperature dependence of ρ, we consider that the semiconducting behavior is due to short-range correlation of Fe^{2+} and Fe^{3+} ions above the CO temperature as discussed for $LuFe_2O_4$ [23,24]. This interpretation is consistent with the small change of activation energy and small ΔS at T_{t1} in comparison with the calculated one $R \ln 2 = 5.76$ J/K · molFe [16].

Magnetic susceptibility M/H exhibits distinct anomalies not only at T_{t1} but also at $T_{t2} = 230$ K, although ρ does not show a clear anomaly at T_{t2}. Here, M is the magnetization and H is the magnetic field. The bottom panel of Fig. 3(a) shows the temperature dependence of M/H of β-$NaFe_2O_3$. Above T_{t2}, M/H is almost field independent. In the high-temperature (HT) phase ($T_{t1} < T$), M/H gradually increases as decreasing T. Then, M/H sharply decreases at T_{t1} and slightly decreases in the intermediate-temperature (IT) phase ($T_{t2} < T < T_{t1}$). At T_{t2}, M/H exhibits a distinct anomaly, and DSC signals show small peak. In the low-temperature (LT) phase ($T < T_{t2}$), M/H has field dependence, and a small spontaneous magnetization appears. The spontaneous magnetization at 200 K was estimated to be approximately 0.01 μ_B/Fe. In addition, the broadening of the ^{23}Na NMR spectrum was observed in the LT phase as shown in Fig. 3(c), indicating a magnetic ordering. The NMR spectrum was well reproduced assuming the internal field 0.06 T at Na sites. The small spontaneous magnetization and small internal field below T_{t2} indicate the occurrence of antiferromagnetic ordering with a slightly canted spin structure. Our preliminary ^{57}Fe Mössbauer measurements also suggest that magnetic ordering occurs below T_{t2}.

B. Charge-ordering pattern

To investigate a structural change associated with CO, we conducted powder SR-XRD measurements at low temperatures. At T_{t1}, a structural transition from the trigonal to monoclinic symmetry occurs. Figure 4 shows the temperature dependence of the unit cell volume V and lattice constants a, b, and c, which are converted to the trigonal cell a_t, b_t, and c_t, respectively. Through the phase transition from the HT phase to the IT phase, a_t and c_t drop, and b_t jumps by about 1%. In contrast, the volume change at T_{t1} is very small, although ΔS is large. In addition, dozens of superlattice reflections were observed below T_{t1} as shown in Fig. 5. The bottom panel of Fig. 4 shows that the integrated intensity of superlattice reflections below T_{t1} increases as T decreases. Although the integrated intensity of superlattice reflections at

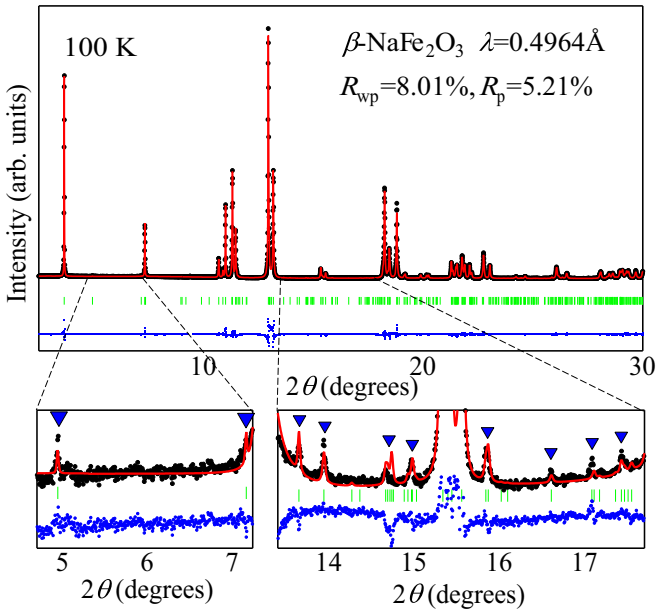

FIG. 5. Synchrotron x-ray diffraction patterns of polycrystalline samples of β-$NaFe_2O_3$ measured at 100 K and the Rietveld fit. Black dots: observed data. Red curves: calculated profiles. Green tick marks: positions of reflections. Blue dots: differences. The bottom section of the figure shows the magnified Rietveld refinement for superlattice reflections. The triangles mark the superlattice reflections.

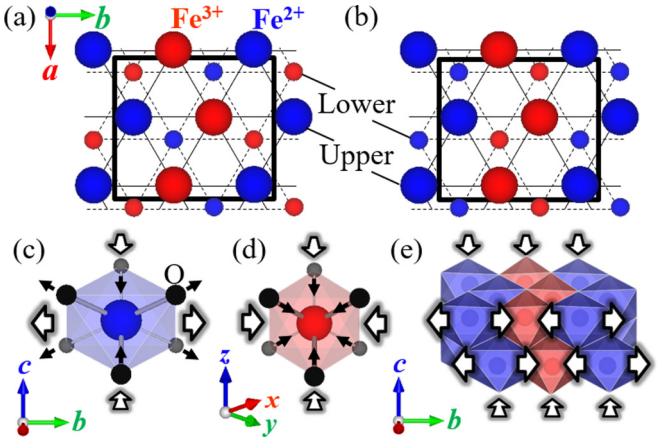

FIG. 6. (a), (b) Two charge-ordering models, (a) Zigzag A and (b) Zigzag B, within a double triangular layer. Solid lines indicate the unit cell. (c) $Fe^{3+}O_6$ octahedron. (d) $Fe^{2+}O_6$ octahedron. Note that these figures represent the general change of FeO_6 octahedra associated with the valence change and Jahn-Teller distortion and do not correspond to the actual displacement of O atoms. The quantization axis (z axis) is shown. (e) Uniaxial deformation of a double triangular layer in Zigzag B.

100 K is approximately 4 orders of magnitude lower than that of fundamental reflections, structural analysis is available by using high-resolution and wide dynamic-range SR-XRD data collected at the BL02B2 beamline [34]. All the superlattice reflections were well indexed with the monoclinic cell: $\vec{a_m} = 2\vec{a_t} + \vec{b_t}$, $\vec{b_m} = 2\vec{b_t}$, and $\vec{c_m} = 2\vec{c_t}$. The inset of Fig. 4 shows the relation between the trigonal cell and the monoclinic cell. Systematic absence of the Bragg reflections is given at $k + l = 2n + 1$ for $h\,k\,l$ indices and $h = 2n + 1$ for $h\,0\,l$ indices. From the above results, the space group below T_{t1} is determined to be $A2/a$, one of the subgroups of $P\bar{3}m1$ in the HT phase. Here, we use the space group $A2/a$ instead of the general notation of $C2/c$ to maintain the direction of the b and c axes in the space group $P\bar{3}m1$ in the HT phase. The following lattice parameters at 100 K are obtained: $a = 5.23447(3)$ Å, $b = 6.18814(4)$ Å, $c = 15.53028(11)$ Å, and $\beta = 90.426(1)^\circ$.

Two CO models are allowed based only on the space group $A2/a$, which are shown in Fig. 6 as Zigzag A and Zigzag B. Each model contains equal amounts of Fe1 and Fe2 sites, which is consistent with our Mössbauer measurement. In a triangular sheet within a W layer, their CO patterns are the same, and two types of Fe zigzag chains alternate along the b axis. The difference between two CO models is the relation between upper and lower triangular sheets owing to the different position of twofold rotation axes in its structure. As shown in Fig. 5, the Rietveld refinement assuming Zigzag B gave good fits to the SR-XRD profile at 100 K. The result of refinements at 100 K is shown in Table II. Since the superlattice intensity is not strong, we verified the validity of Zigzag B by using ^{23}Na NMR techniques. Here, we focus on the difference of site symmetries of Na sites in these two models. The number of crystallographically independent Na sites is 2 and 1 for Zigzag A and Zigzag B, respectively. Assuming one crystallographic Na site, NMR spectra in all the phases were well reproduced as shown in Fig. 3(c). Both NMR and SR-XRD measurements support Zigzag B.

The volume of FeO_6 octahedra clearly changes accompanied by CO. The average bond length of $Fe1O_6$ and $Fe2O_6$ octahedra at 100 K is approximately 2% shorter and longer than that at 300 K, respectively. Based on the bond valence sum calculation [36], the valences for Fe1 and Fe2 sites at 100 K are estimated to be 2.63 and 2.02, respectively. The results of structural analysis are consistent with the CO picture.

TABLE II. Refined structural parameters for β-$NaFe_2O_3$ at 100 K determined using synchrotron x-ray diffraction patterns. The space group is $A2/a$, and the obtained lattice parameters are $a = 5.23447(3)$ Å, $b = 6.18814(4)$ Å, $c = 15.53028(11)$ Å, and $\beta = 90.426(1)^\circ$. The obtained R factors are R_{wp}=8.01%, R_p=5.21%. The same values of isotropic temperature factors B were given for oxygen atoms (B(O1)=B(O2) and B(O3)=B(O4)). Here, O1 and O2 in the monoclinic cell are the symmetry-related pairs of O1 in the trigonal cell, and O3 and O4 in the monoclinic cell are the symmetry-related pairs of O2 in the trigonal cell.

Atom	Site	x	y	z	B (Å^2)
Na	8f	0.2472(18)	0.6272(30)	0.2472(4)	0.71(4)
Fe1	8f	0.9183(5)	0.6253(11)	0.4147(1)	0.09(3)
Fe2	8f	0.9161(5)	0.6248(10)	0.9180(1)	0.14(3)
O1	4e	1/4	0.110(5)	0	0.85(9)
O2	4e	1/4	0.655(3)	0	0.85(9)
O3	8f	0.9008(15)	0.6401(25)	0.1452(5)	0.15(6)
O4	8f	0.9183(16)	0.6104(26)	0.6521(5)	0.15(6)

C. The origin of electrostatically unstable charge ordering

In terms of Coulomb interactions, Zigzag B is seemingly less stable than Zigzag A. Zigzag A satisfies Anderson's condition that each Fe_4 tetrahedron of four neighboring sites should contain two Fe^{2+} and two Fe^{3+} ions considering local Coulomb repulsions on Fe_4 tetrahedra [15]. In the CO pattern satisfying Anderson's condition, a large $Fe^{2+}O_6$ octahedron and a small $Fe^{3+}O_6$ octahedron are spatially arranged as far apart as possible, which can decrease lattice distortions. In contrast, Zigzag B does not satisfy Anderson's condition, which suggests an electrostatically unstable CO pattern. Furthermore, Zigzag A is present in the theoretical phase diagram, considering long-range Coulomb repulsions within a W layer, while Zigzag B is absent [37,38]. The stability of Zigzag B cannot be explained using a simple model. Electrostatically unstable CO patterns are sometimes reported in mixed-valent iron oxides [18,39]. It is expected that a hidden mechanism stabilizes such CO patterns in these compounds.

Here, we discuss the inherent degrees of freedom in the HT phase to drive the phase transition at T_{t1} in β-$NaFe_2O_3$. Since β-$NaFe_2O_3$ does not show magnetic ordering in the HT phase, β-$NaFe_2O_3$ has spin degrees of freedom. However, the coupling between charge and spin degrees of freedom is expected to be weak, since CO and magnetic ordering occur at different temperatures, which is commonly observed in mixed-valent iron oxides [17,20–23,39,40]. Thus, we conclude that spin degrees of freedom do not significantly influence on CO. Next, we focus on orbital states in the HT phase. In the HT phase, the distortion of FeO_6 octahedra is small, suggesting a triply degenerate t_2 orbital. Thus, orbital degrees of freedom are present for the d^6 configuration of high-spin Fe^{2+} ions in β-$NaFe_2O_3$, while they are absent for the d^5 configuration of Fe^{3+} ions.

Here, we focus on the distortion of $Fe^{2+}O_6$ octahedra of β-$NaFe_2O_3$ in the CO state. The average length of two Fe-O bonds along the z axis (quantization axis) at 100 K is approximately 8% shorter than that of the other four bonds. A schematic drawing is shown in Fig. 6(c), which shows the direction of the z axis. This deformation corresponds to tetragonal Jahn-Teller (JT) compression that stabilizes an extra single electron occupying one of three t_2 orbitals. Such a tetragonal JT compression often occurs at CO temperature as reported in some mixed-valent iron oxides with $Fe^{2.5+}$ ions [18,39,41].

On the basis of symmetry operations in Zigzag B, all the z axes in $Fe^{2+}O_6$ octahedra point in the same direction, which suggests the ferro-orbital arrangement. Thus, all the $Fe^{2+}O_6$ octahedra expand along the b axis and shrink along the z axis.

The ferro-orbital arrangement of Fe^{2+} ions is the key to the stability of Zigzag B. Considering JT distortion of $Fe^{2+}O_6$ octahedra, double-stripe chains consisting of Fe^{2+} ions shrink along the z-axis. Double-stripe chains consisting of Fe^{3+} ions also shrink along the z axis, since all the $Fe^{3+}O_6$ octahedra become small, owing to the valence change as shown in Fig. 6(d). The cooperative compression along the z axis decreases the energy loss of distortion. A schematic drawing of the deformation of a W layer is shown in Fig. 6(e). One important point is that all the $Fe^{2+}O_6$ octahedra expand along the b axis. Owing to the stripe-type valence arrangement, the expansion of $Fe^{2+}O_6$ octahedra does not significantly deform the Fe^{3+} octahedra. This uniaxial deformation is consistent with the decrease in a and increase in b at T_{t1} shown in Fig. 4. This is one reason why the cell volume change associated with CO is small, resulting in the small energy loss of distortion. Thus, electron-phonon interactions play a significant role on the CO transition in β-$NaFe_2O_3$.

The magnetic properties are consistent with CO accompanied by ferro-orbital arrangement of Fe^{2+} ions. The antiferromagnetic arrangement below T_{t2} can be explained by the ferro-orbital arrangement of Fe^{2+} ions, since antiferromagnetic interactions are dominant between Fe^{2+} ions based on the Kugel-Khomskii theory [42]. The drop of M/H at T_{t1} as T decreases likely originates from the enhancement of short-range antiferromagnetic interactions between Fe ions and/or the increase in magnetocrystalline anisotropy, owing to the existence of Fe^{2+} ions. Furthermore, M/H in the IT phase gradually decreases as T decreases, despite the semiconductor. This result suggests the increase in antiferromagnetic interaction and/or magnetocrystalline anisotropy originating from a gradual structural change.

Although β-$NaFe_2O_3$ and $LuFe_2O_4$ have similar W layers, their CO patterns are different. The difference can originate from the different coordination environment of Fe ions: FeO_6 octahedra for β-$NaFe_2O_3$ and FeO_5 bipyramids for $LuFe_2O_4$. Thus, JT effects of β-$NaFe_2O_3$ are significantly different from those of $LuFe_2O_4$.

The origin of the unusual double-stripe CO pattern of β-$NaFe_2O_3$ can be summarized as follows. The CO pattern is determined to minimize a distortion of W layers caused by the deformation of FeO_6 octahedra, owing to the valence change and JT distortion. Our results clarify the importance of electron-phonon coupling in the CO transition. Unusual CO phenomena are often observed in geometrically frustrated compounds, such as Fe_3O_4 and $LuFe_2O_4$ [18–21], in which energy gain mediated by long-range Coulomb interactions in the CO state is small, owing to charge frustration. As a result, cooperative effects of Coulomb repulsions and relatively large electron-phonon interactions induce anomalous CO phenomena. Our experimental results will help to clarify the origin of unusual CO phenomena observed in mixed-valent oxides with charge frustration.

IV. SUMMARY

Polycrystalline β-$NaFe_2O_3$ was synthesized and characterized using the following techniques: SR-XRD, magnetization, electrical resistivity, DSC, ^{23}Na NMR, and ^{57}Fe Mössbauer measurements. β-$NaFe_2O_3$ exhibits charge ordering at 250 K and antiferromagnetic ordering with a slightly canted spin structure at 230 K. β-$NaFe_2O_3$ shows a double-stripe-type charge-ordering pattern of Fe^{2+} and Fe^{3+} ions. This arrangement does not satisfy Anderson's condition of minimal electrostatic repulsions, suggesting that it is electrostatically unstable. The cooperative compression of $Fe^{3+}O_6$ and $Fe^{2+}O_6$ octahedra stabilizes the electrostatically unstable double-stripe charge-ordering pattern. Our experimental results indicate the importance of electron-phonon coupling in the region of strong

charge frustration, which is key to clarifying the origin of the electrostatically unstable charge ordering often observed in mixed-valent iron oxides.

ACKNOWLEDGMENTS

The authors thank S. Kawaguchi, A. Nakano, and S. Kitou for supporting the SR-XRD measurements, M. Imai for supporting the analysis of NMR data, and N. Katayama for helpful discussion. This work was partially carried out using the facilities of Research Center for Low Temperature and Materials Sciences, Kyoto University. The synchrotron radiation experiments were performed at the BL02B2 of SPring-8 with the approval of the Japan Synchrotron Radiation Research Institute (JASRI) (Proposal No. 2016A1620 and 2016B1437). This work was supported by JSPS KAKENHI Grants No. 14J01400, No. 16J04046, and No. 16H04131. The figures of crystal structure were created using VESTA [43]. Rietveld analyses were conducted using the GSAS program [44].

[1] P. W. Anderson, Mater. Res. Bull. **8**, 153 (1973).
[2] L. Balents, Nature **464**, 199 (2010).
[3] A. P. Ramirez, G. P. Espinosa, and A. S. Cooper, Phys. Rev. Lett. **64**, 2070 (1990).
[4] Y. Shimizu, K. Miyagawa, K. Kanoda, M. Maesato, and G. Saito, Phys. Rev. Lett. **91**, 107001 (2003).
[5] T. Kakiuchi, Y. Wakabayashi, H. Sawa, T. Itou, and K. Kanoda, Phys. Rev. Lett. **98**, 066402 (2007).
[6] H. Seo and Y. Motome, Phys. Rev. Lett. **102**, 196403 (2009).
[7] F. Kagawa, T. Sato, K. Miyagawa, K. Kanoda, Y. Tokura, K. Kobayashi, R. Kumai, and Y. Murakami, Nat. Phys. **9**, 419 (2013).
[8] S. Sasaki, K. Hashimoto, R. Kobayashi, K. Itoh, S. Iguchi, Y. Nishio, Y. Ikemoto, T. Moriwaki, N. Yoneyama, M. Watanabe, A. Ueda, H. Mori, K. Kobayashi, R. Kumai, Y. Murakami, J. Müller, and T. Sasaki, Science **357**, 1381 (2017).
[9] T. Sato, K. Miyagawa, and K. Kanoda, Science **357**, 1378 (2017).
[10] Y. Okamoto, S. Niitaka, M. Uchida, T. Waki, M. Takigawa, Y. Nakatsu, A. Sekiyama, S. Suga, R. Arita, and H. Takagi, Phys. Rev. Lett. **101**, 086404 (2008).
[11] P. G. Radaelli, Y. Horibe, M. J. Gutmann, H. Ishibashi, C. H. Chen, R. M. Ibberson, Y. Koyama, Y.-S. Hor, V. Kiryukhin, and S.-W. Cheong, Nature **416**, 155 (2002).
[12] K. Matsuno, T. Katsufuji, S. Mori, Y. Moritomo, A. Machida, E. Nishibori, M. Takata, M. Sakata, N. Yamamoto, and H. Takagi, J. Phys. Soc. Jpn. **70**, 1456 (2001).
[13] Y. Horibe, M. Shingu, K. Kurushima, H. Ishibashi, N. Ikeda, K. Kato, Y. Motome, N. Furukawa, S. Mori, and T. Katsufuji, Phys. Rev. Lett. **96**, 086406 (2006).
[14] E. J. W. Verwey, Nature **144**, 327 (1939).
[15] P. W. Anderson, Phys. Rev. **102**, 1008 (1956).
[16] E. F. Westrum, Jr. and F. Grønvold, J. Chem. Thermodyn. **1**, 543 (1969).
[17] P. A. Miles, W. B. Westphal, and A. Von Hippel, Rev. Mod. Phys. **29**, 279 (1957).
[18] M. S. Senn, J. P. Wright, and J. P. Attfield, Nature **481**, 173 (2012).
[19] J. P. Wright, J. P. Attfield, and P. G. Radaelli, Phys. Rev. Lett. **87**, 266401 (2001).
[20] F. Walz, J. Phys.: Condens. Matter **14**, R285 (2002).
[21] N. Ikeda, H. Ohsumi, K. Ohwada, K. Ishii, T. Inami, K. Kakurai, Y. Murakami, K. Yoshii, S. Mori, Y. Horibe, and H. Kitô, Nature **436**, 1136 (2005).
[22] Y. Yamada, K. Kitsuda, S. Nohdo, and N. Ikeda, Phys. Rev. B **62**, 12167 (2000).
[23] M. Angst, Phys. Status Solidi RRL **7**, 383 (2013).
[24] M. Angst, R. P. Hermann, A. D. Christianson, M. D. Lumsden, C. Lee, M.-H. Whangbo, J.-W. Kim, P. J. Ryan, S. E. Nagler, W. Tian, R. Jin, B. C. Sales, and D. Mandrus, Phys. Rev. Lett. **101**, 227601 (2008).
[25] M. Tanaka, K. Siratori, and N. Kimizuka, J. Phys. Soc. Jpn. **53**, 760 (1984).
[26] S. Lafuerza, J. García, G. Subías, J. Blasco, K. Conder, and E. Pomjakushina, Phys. Rev. B **88**, 085130 (2013).
[27] J. Blasco, S. Lafuerza, J. García, and G. Subías, Phys. Rev. B **90**, 094119 (2014).
[28] J. de Groot, T. Mueller, R. A. Rosenberg, D. J. Keavney, Z. Islam, J.-W. Kim, and M. Angst, Phys. Rev. Lett. **108**, 187601 (2012).
[29] D. Niermann, F. Waschkowski, J. de Groot, M. Angst, and J. Hemberger, Phys. Rev. Lett. **109**, 016405 (2012).
[30] V. Markovich, I. Fita, A. Wisniewski, R. Puzniak, C. Martin, G. Jung, and G. Gorodetsky, Phys. Rev. B **96**, 054416 (2017).
[31] A. M. E. Balkhi, A. Courtois, M. Zanne, and C. Gleitzer, C. R. Acad. Sci. C. Chim. **285**, 129 (1977).
[32] A. M. E. Balkhi, M. Zanne, C. Gleitzer, and A. Courtois, J. Solid State Chem. **18**, 293 (1976).
[33] S. R. Bruno, C. K. Blakely, and V. V. Poltavets, J. Solid State Chem. **192**, 68 (2012).
[34] S. Kawaguchi, M. Takemoto, K. Osaka, E. Nishibori, C. Moriyoshi, Y. Kubota, Y. Kuroiwa, and K. Sugimoto, Rev. Sci. Instrum. **88**, 085111 (2017).
[35] See Supplemental Material at http://link.aps.org/supplemental/10.1103/PhysRevMaterials.2.054402 for analysis procedure and explanation of ^{23}Na NMR and ^{23}Fe Mössbauer measurements.
[36] I. Brown and D. Altermatt, Acta Crystallogr. Sect. B **41**, 244 (1985).
[37] M. Naka, A. Nagano, and S. Ishihara, Phys. Rev. B **77**, 224441 (2008).
[38] A. Nagano, M. Naka, J. Nasu, and S. Ishihara, Phys. Rev. Lett. **99**, 217202 (2007).
[39] P. M. Woodward and P. Karen, Inorg. Chem. **42**, 1121 (2003).
[40] J. Attfield, A. Bell, L. Rodriguez-Martinez, J. Greneche, R. Cernik, J. Clarke, and D. Perkins, Nature **396**, 655 (1998).
[41] M. Angst, P. Khalifah, R. P. Hermann, H. J. Xiang, M.-H. Whangbo, V. Varadarajan, J. W. Brill, B. C. Sales, and D. Mandrus, Phys. Rev. Lett. **99**, 086403 (2007).
[42] K. I. Kugel and D. I. Khomskii, Sov. Phys. Usp. **25**, 231 (1982).
[43] K. Momma and F. Izumi, J. Appl. Crystallogr. **44**, 1272 (2011).
[44] B. H. Toby, J. Appl. Cryst. **34**, 210 (2001).